Soft Matter

Accepted Manuscript

This is an *Accepted Manuscript*, which has been through the Royal Society of Chemistry peer review process and has been accepted for publication.

Accepted Manuscripts are published online shortly after acceptance, before technical editing, formatting and proof reading. Using this free service, authors can make their results available to the community, in citable form, before we publish the edited article. We will replace this *Accepted Manuscript* with the edited and formatted *Advance Article* as soon as it is available.

You can find more information about *Accepted Manuscripts* in the Information for Authors.

Please note that technical editing may introduce minor changes to the text and/or graphics, which may alter content. The journal's standard Terms & Conditions and the Ethical guidelines still apply. In no event shall the Royal Society of Chemistry be held responsible for any errors or omissions in this *Accepted Manuscript* or any consequences arising from the use of any information it contains.

ROYAL SOCIETY OF CHEMISTRY

www.rsc.org/softmatter

Journal Name

ARTICLE TYPE

Cite this: DOI: 10.1039/xxxxxxxxxx

Dynamics of colloid accumulation under flow over porous obstacles†

Matthieu Robert de Saint Vincent,*[a] Manouk Abkarian, [b] and Hervé Tabuteau[a]

Received Date
Accepted Date

DOI: 10.1039/xxxxxxxxxx

www.rsc.org/journalname

The accumulation of colloidal particles to build dense structures from dilute suspensions may follow distinct routes. The mechanical, structural and geometrical properties of these structures depend on local hydrodynamics and colloidal interactions. Using model suspensions flowing into microfabricated porous obstacles, we investigate this interplay by tuning both the flow pattern and the ionic strength. We observe the formation of a large diversity of shapes, and demonstrate that growing structures in turn influence the local velocity pattern, favouring particle deposition either locally or over a wide front. We also show that these structures are labile, stabilised by the flow pushing on them, in low ionic strength conditions, or cohesive, in a gel-like state, at higher ionic strength. The interplay between aggregate cohesion and erosion thus selects preferential growth modes and therefore dictates the final shape of the structure.

1 Introduction

Various strategies have been used to form dense structures of colloidal particles from suspensions with a low particle concentration. In most cases, the particles are driven either by a bulk force or by a flow towards a zone where they eventually accumulate. The most common example bulk force is gravity which drives accumulation at the bottom of containers by sedimentation of particles denser than the suspending fluid. Since this process is slow, the Péclet number, Pe, is small and diffusion dominates the piling-up dynamics. The structure of the deposit thus only depends on the interparticle potential. Hard and charge-stabilised spheres pack into a dense ordered deposit, *i.e.* a colloidal crystal[1], while weakly attractive systems, by depletion forces for instance, form tenuous gels[2]. In the case of flow-driven assembly, a well known example is the building-up of a ring-shaped stain during the drying of a colloidal dispersion droplet deposited over a substrate[3]. Here, the accumulation rate increases with the driving force, *i.e.* the evaporative flux towards the contact line. Particles form a crystal at low fluxes, while stronger flows lead to amorphous disordered packings[4].

To access a wider range of Péclet numbers in flow-driven accumulation, Kusaka *et al.* flowed particles in a microfluidic channel and accumulated them on an obstacle, a cylindrical collector placed within the flow path[5]. They imposed a high ionic strength to completely screen the charge of both the PDMS channel and the particles. For $0.3 < \mathrm{Pe} < 50$, deposits are nearly uniform on the upstream half of the obstacle, whereas at $\mathrm{Pe} > 100$, the deposit sharpens up to a finger-like shape. A similar aggregate shape was also observed by Bacchin *et al.* at the entrance of a microfluidic filter, also in high ionic strength conditions[6,7]. Ortiz *et al.* performed similar experiments at very high confinement (channel 1.6 particle diameter high), using a slender porous obstacle, perpendicular to the flow direction[8]. They showed that a heap of particles reversibly builds up on the obstacle at low Pe. Since the polystyrene particles were charge-stabilised, the heap behaves as a dense repulsive glass, held stable by a sufficient permeation flow. Indeed, they observed numerous rearrangements within the heap, and the structure entirely dissolved when the flow was turned off. In a companion paper, they used the same set up with weakly attractive particles[9]. The overall shape of the heap was observed similar to the repulsive case but this time it corresponds to a colloidal gel featuring elastic properties.

In all the above mentioned studies, the mechanical, structural and geometrical properties of dense structures built by retention of colloids are expected to depend on the interplay between hydrodynamic and colloidal interactions. However, from these investigations it is difficult to define clearly how those two phenomena are related. Indeed, they focused primarily on the influence of the flow but considered different obstacle geometries; the influence of ionic strength was not specifically studied. In the present paper, we investigate this interplay by characterising the growth of dense structures (hereafter referred to as aggregates) over microfabricated constrictions. By tuning both the inflow velocity

[a] IPR, UMR CNRS 6251, Campus Beaulieu, Université Rennes 1, 35042 Rennes, France. E-mail: rdsv.matthieu@gmail.com
[b] L2C, UMR CNRS 5221, Université Montpellier 2, 34095 Montpellier, France.

† Electronic Supplementary Information (ESI) available: Estimate of Péclet numbers; computed velocity and velocity gradient profiles; movies illustrating the aggregate growth and withdrawn. Three figures, seven movies. See DOI: 10.1039/b000000x/

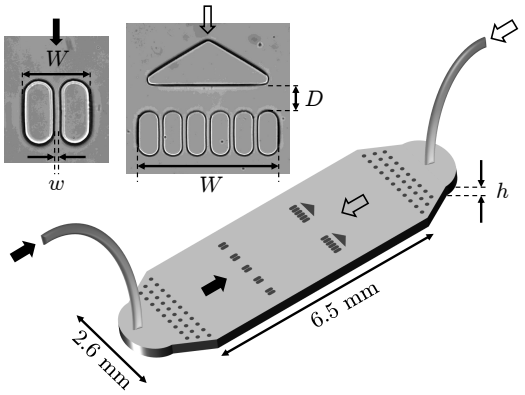

Fig. 1 Sketch of the microfluidic device used throughout this study. Two types of porous obstacles, referred to as single (left) and sheltered (right) pores, are placed head to tail into the channel. The aggregation over single and sheltered pores is selectively studied by injecting suspensions through either (filled or open arrows) inlet.

and the interparticle electrostatic repulsion, we observe a large diversity of aggregate shapes, and characterise their growth dynamics. Computer simulations of the local flow near the constriction show how hydrodynamic forces drive the localised particle deposition, and how the growing aggregate in turn influences the flow field. We then use a dedicated obstacle geometry to favour the formation of larger aggregates. We evidence by this way a structural transition from a liquid-like state to an aggregated, solid-like state, when decreasing the electrostatic repulsion. This transition allows to discuss the observed aggregate shapes through the interplay between DLVO (Derjaguin, Landau, Verwey and Overbeek) colloidal interactions[10] and hydrodynamic drag. We thus distinguish three main regimes of particle aggregation: labile, cohesive without significant erosion, cohesive and eroded.

2 Experimental procedure

We carried out experiments by flowing suspensions within polydimethylsiloxane (PDMS) microfluidic channels, moulded by standard soft lithography techniques[11] and sealed onto PDMS-coated glass slides. Channels are typically $h = 16$-μm high and millimetric in length and width (Hele-Shaw geometry), which allows to consider a nearly flat velocity profile along the channel width[12]. We considered two distinct obstacle shapes, represented on Fig. 1. The first shape, referred to as 'single pore' (see left image in Fig. 1), is composed of two elongated collectors, separated by a gap of width $w = 10$ μm and ended with spherical caps (total width of the obstacle, $W = 70$ μm). The second shape, called 'sheltered pore', consists of three parallel single pores ($W = 230$ μm), covered with a triangular obstacle placed upstream at a variable distance D (Fig. 1, right image). These two designs allow to modulate the velocity gradient, and therefore to consider high- and low-shear regimes of particle accumulation. Multiple obstacles of each type are drawn on a line orthogonal to the main flow (eight single pores in a line, four sheltered pores in another) to follow several aggregate growths in parallel. Each pore geometry can be selectively used by flowing the suspension from either inlet, as shown on Fig. 1 (filled or open arrows for single or sheltered pores, respectively).

Dilute colloidal suspensions (volume fraction ϕ ranging from 2×10^{-4} to 10^{-3}) were prepared by suspending polystyrene microspheres (Invitrogen, diameter 4 μm ± 8 %) with 1 mM EDTA (to prevent bacterial growth) in ultrapure water (also used to flush the channel prior to any particle injection). Particles are stabilised by long-range electrostatic repulsion due to sulfate groups producing a negative surface charge (zeta potential −32 mV at pH 7). We screened this repulsive interaction by tuning the ionic strength I of the suspension, adding NaCl at concentrations up to 50 mM (the critical coagulation concentration is 70 mM). Care was taken to avoid the presence of aggregates by sonicating the suspensions for at least 30 min prior to experiments; finally, networks of collectors placed after each inlet act as filters retaining residual bigger objects. The suspensions are then fed, and may be withdrawn after experiments, at a constant flow rate Q (in the range 5–500 μL min^{-1}) by a Harvard Apparatus PHD 2000 syringe pump. Using Comsol Multiphysics software, we then computed the velocity map around a pore, and deduced the corresponding Péclet numbers at the entrance of an empty pore, Pe (see Supplementary Material†, section S1, for details), which were found in the range 375–1.5×10^5 in single pores and 119–1.0×10^4 in sheltered pores for the considered flow rates (Supplementary Figure S1†).

Finally, the system was imaged in bright-field microscopy on an inverted microscope (Leica, ×40 objective lens) equipped with a motorised stage to allow a sequential scanning (temporal resolution up to 4 s) over a full line of pores. Digital images were recorded (Hamamatsu Orca Flash 4.0 camera) and further analysed with a home-written macro in ImageJ[13] to extract aggregates shape and surface area.

3 The high-shear regime: Aggregate growth over a single pore

Experiments start when each individual pore is clogged by particles[14], allowing the subsequent accumulation of particles to take place. As the parallel pores did not clog simultaneously, the origin of time was individually set when the front of particle accumulation approximately coincided with the apex of the pore [see dashed line on Fig. 2 (a)]. The total duration of an experiment typically ranges from 10 min to 3 h depending on the volume fraction and flow rate used. To directly compare experiments, we systematically calculated the number N of particles flowing through the cross section $W \times h$ of an obstacle. We first focus on the single pore case.

3.1 Final aggregate shapes

Highly-repulsive particles ($I = 0$ mM) rapidly accumulate to build a small corner-shaped aggregate, of 3–4 particles in side length, centred on the pore axis as represented on Fig. 2 (b) for two flow rates. Secondary deposits may also grow, though not systematically, over the pore apex, which are not considered here as they are not connected with the central aggregate. This triangular shape, hereafter referred to as 'corner', is typically reached after $N \simeq 10^5$ particles have encountered the pore, and does not

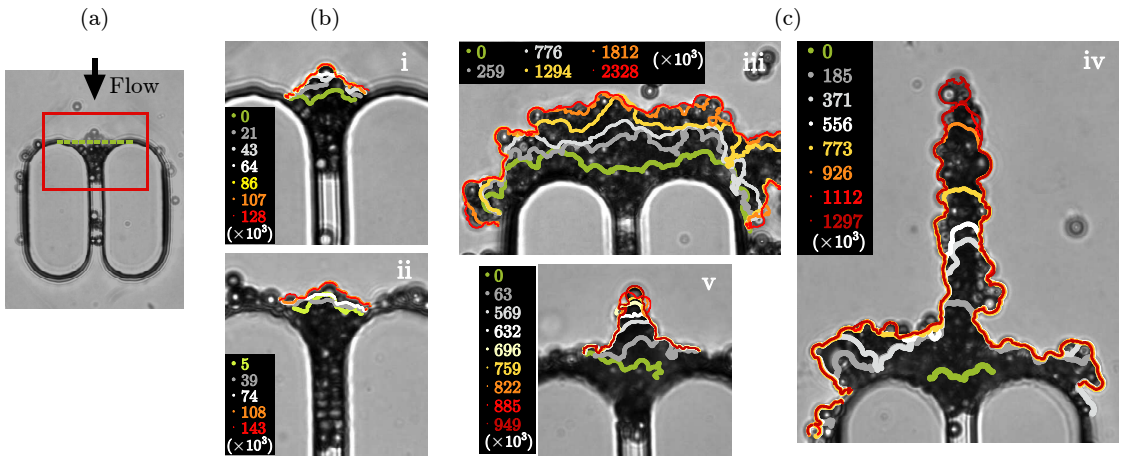

Fig. 2 Typical images illustrating the aggregate shapes obtained over a single pore when varying the ionic strength and flow rate. The box in (a) illustrates the cropped area considered on the images. The origin of time was set when the growing front approximately coincided with the apex of the pore (dashed line). (b) $I = 0$ mM, Pe $= 781$ (i) and 1.3×10^4 (ii), shape: corner; (c) $I = 50$ mM, Pe $= 1.7 \times 10^3$ (iii, shape: flat), 3.5×10^4 (iv, shape: finger) and 1.5×10^5 (v, shape: tip). Representative profiles corresponding to increasing numbers of flowing particles are superimposed to the images to illustrate the aggregate growth.

significantly evolve afterwards although internal rearrangements may occur at the single particle scale (see Supplementary Movie 1†). Interestingly, both the steady shape and the growth dynamics seem quite independent of the imposed flow rate (compare profiles on images i and ii). Note that although the depth of the clog may vary from pore to pore, as seen on the two images, we did not notice it impacts the aggregate shape significantly.

In contrast, the shape of the aggregate changes with the Péclet number at high ionic strength [Fig. 2 (c), $I = 50$ mM; see also Supplementary Movies 2–4†]. At a low Pe (781, image iii), particles accumulate over a wide, poorly defined front, and the aggregate keeps growing even when $N > 2 \times 10^6$ particles. This shape is referred to as 'flat'. Increasing Pe (3.5×10^4), an elongated aggregate ('finger') grows along the pore axis (image iv). In this case, the growth is continuous (though rather fluctuating in time) along the pore centreline, on top of a wider basis initially formed by collection of particles on the pore apex. Finally, at even higher Pe (1.5×10^5, image v) a shorter and sharper shape ('tip') forms along the centreline. However, contrary to the previous case, the growth saturates rather quickly, and the shape of the extremity permanently oscillates due to a succession of deposition and erosion of single particles (compare the successive profiles over 8×10^5 particles).

3.2 Growth dynamics

The various shapes described above suggest that the growth may follow different routes when varying the experimental parameters (Pe and I), in line with observations reported in the literature[5,8]. To characterise them more quantitatively, we first measured the evolution of the area $\mathscr{A}$ of the aggregate built over the clog. Figure 3 (a) represents the aggregate growth dynamics in the $I = 0$ mM case (corner shape), for four different Péclet numbers spanning almost three orders of magnitude. The growth, initially fast, progressively slows down and finally saturates around 120 μm^2. Despite the large amplitude of flow rate variation, the

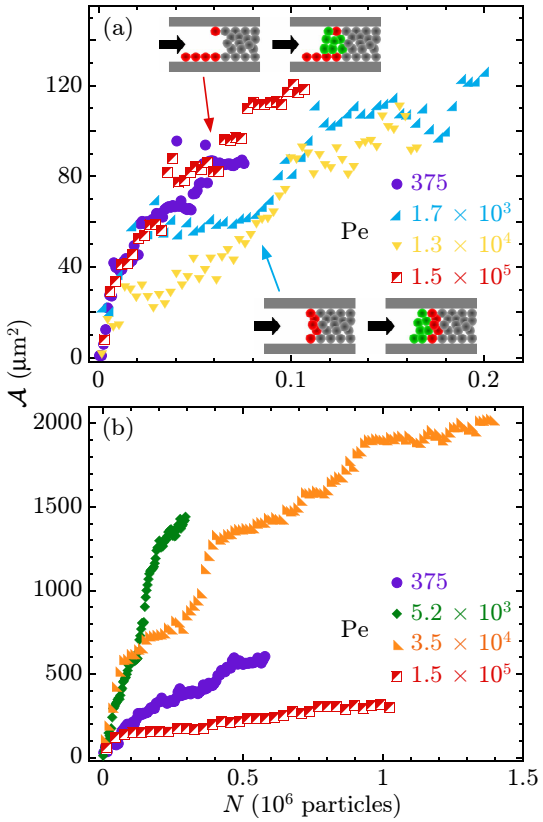

Fig. 3 Aggregate growth dynamics over a single pore, for several values of Pe. The cumulated area $\mathscr{A}$ corresponds to the structure built upon the apex front, as represented in light grey on Fig. 2 (a). Each dynamics corresponds to a single aggregate growth; areas measured over four parallel single pores typically varied by ±15 %. (a) $I = 0$ mM, (b) $I = 50$ mM. Insets in (a): cartoons illustrating the two different capture scenarios discussed in the text (side view); black arrows indicate the flow direction.

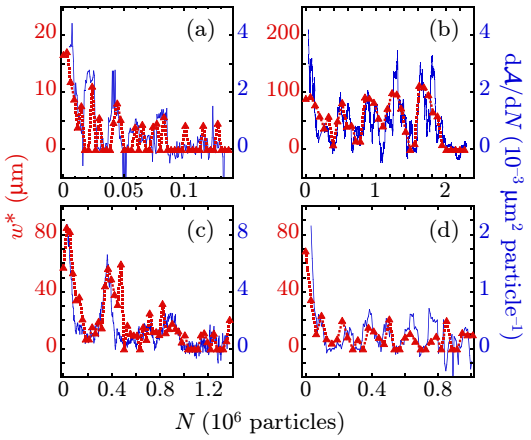

Fig. 4 Temporal evolution of the effective capture front w^* (dotted-line-connected symbols) and the aggregate growth rate (running mean of the derivative of the cumulated surface, solid line), for the four typical shapes illustrated on Fig. 2. (a) Corner, $I = 0$ mM, Pe $= 781$, (b) flat, $I = 50$ mM, Pe $= 1.7 \times 10^3$, (c) finger, $I = 50$ mM, Pe $= 3.5 \times 10^4$, (d) tip, $I = 50$ mM, Pe $= 1.5 \times 10^5$.

four dynamics are quite comparable, although the growth may follow distinct paths, rather fast and continuous (Pe $= 375$ and 1.5×10^5) or more jerky (1.3×10^4). These paths may correspond to distinct capture scenarios, sketched in the two insets of Fig. 3 (a). In the former case, particles would first deposit on the surface, then build a 3D aggregate by capture in the bulk, resulting in a fast initial growth of the measured area that rapidly saturates while the captured particles are hidden by surface deposits (upper inset). In the latter case, particles would simultaneously be captured on the surface and in the bulk, resulting in an apparently slower, layer-by-layer build-up (lower inset). However, the final shape remains similar in both cases, regardless of the growth scenario, which suggests that the aggregate structure is the same.

In contrast, the $I = 50$ mM case, represented on Fig. 3 (b), features clearly distinct behaviours as anticipated from the experimental images. At low Pe (375 and 5.2×10^3), corresponding to flat-shaped aggregates, the growth is fairly linear, though the growth rate strongly varies with the inflow speed. A higher flow rate (corresponding to Pe $= 3.5 \times 10^4$, finger shape) features an alternation between fast and slower growths, but the aggregate build-up continues over the whole duration of the experiment. Finally, at the highest investigated flow rate (Pe $= 1.5 \times 10^5$, tip shape) the growth resembles more to the $I = 0$ mM case, featuring a fast initial growth followed by a saturation; the succession of erosion and deposition can also be noted through the final oscillations of the area.

3.2.1 Location of the particle capture.

Growth dynamics strongly varies from shape to shape. One may then expect that shape affects the effective capture front, w^*, corresponding to the cross width over which incident particles may be captured. We therefore measured the maximal width over which particles got captured during a time interval Δt. For instance, $w^* = W$ if the particles captured between times t and $t + \Delta t$ span the whole width of the pore, no matter how many particles effectively got captured; conversely, no deposition returns $w^* = 0$. In Fig. 4 (a–d), the red dotted-line-connected symbols depict the evolution of w^* with N for the four shapes illustrated on Fig. 2.

In addition, we estimated the evolution of the aggregate growth rate by calculating the derivative of its area with respect to N. This evolution is also plotted on Fig. 4 (a–d), blue solid line — a running mean of the derivative is actually plotted to smooth short-time variations. We clearly see that w^* and $d\mathcal{A}/dN$ are well correlated as will be discussed in section 3.2.3.

The 'corner' case [Fig. 4 (a)] is characterised by a rapid decrease of the capture front, from about four particles (16 µm) to zero, with punctual jumps corresponding to the capture of a single additional particle in the saturated regime. This capture may occur after an internal rearrangement or erosion have created an unoccupied deposition site.

In the 'flat' case [Fig. 4 (b)], the capture proceeds over a front which can be wider than W (up to 100 µm), long after the initial deposition. Three main temporal patterns may actually be observed. At low Pe (781 or less), the capture is sporadic, featuring almost no deposition most of the time and punctual deposition events over a wide front, without apparent periodicity. At higher flow rate (Pe $= 1.7 \times 10^3$), the deposition becomes more continuous, in the sense that deposition always occurs, though irregularly. Finally, another alternating regime can be observed at high flow rate (Pe $= 1.7 \times 10^3$) and salinity ($I = 50$ mM). In this regime [see Fig. 4 (b)], the alternation between wide front and localised capture (over 1–2 particle diameters) is remarkably periodic. Note finally that the maximal value of w^* increases at each oscillation, which suggests that the aggregate grows laterally as well as frontally: particles are captured at the edge of the existing aggregate and create by this way additional capture sites.

The 'finger' case [Fig. 4 (c)] is characterised by the building up of a wide base ($N < 2 \times 10^5$ particles), followed by a quite continuous growth over a 3–4-particle wide front. The peak near 3×10^5 particles corresponds to the capture of a residual big object on the left shoulder (see Fig. 2, image iv) that retains additional particles on the base.

Finally, the 'tip' case is represented on Fig. 4 (d). Here, the capture front periodically oscillates between 0 (no capture) and 2–3 particle diameters. We also note the erosion ($d\mathcal{A}/dN < 0$) of single particles at the extremity.

3.2.2 Local flow patterns.

The aggregate growth dynamics is related to the location of the particle capture, which likely depends on the hydrodynamic forces and torques experienced by an incident particle. To characterise the influence of the aggregate on local hydrodynamics, we computed the flow pattern near the pore entrance for different aggregate geometries.

When our experiments start ($N = 0$), clogged pores still allow a permeation flow through the porous clog. We simulated this porosity by inserting a network of obstacles within the pore entrance (as sketched on Supplementary Figure S2†and in the inset of Fig. 5). From the velocity map, we more specifically calculated the axial and transverse velocity gradients, $\partial v/\partial y$ and $\partial v/\partial x$, over a so-called 'interception' line, transverse to the flow and located

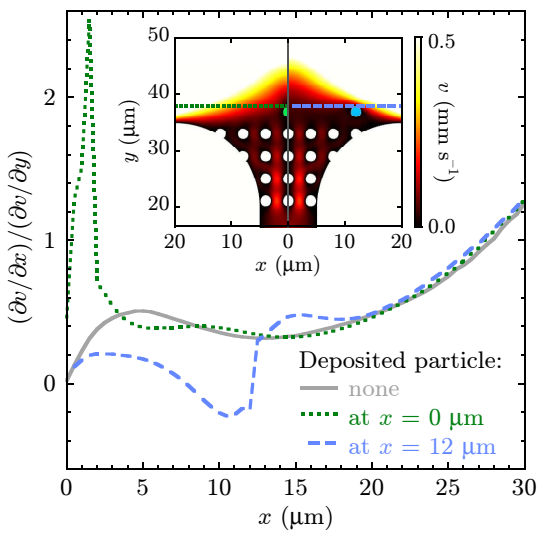

Fig. 5 Profile of the transverse-to-axial ratio of velocity gradients along the interception line, at three stages of the particle deposition history (no particle deposited, central deposition, lateral deposition). Inset: Velocity map computed in the vicinity of the pore entrance for an inflow velocity $v_0 = 8$ mm s^{-1} (corresponding to $Q = 20$ µL min^{-1} or Pe $= 1.7 \times 10^3$), when a particle is deposited at $x = 0$ (left half) and 12 µm (right half). The dotted and dashed lines depict the interception line in the central and lateral deposition cases, respectively. The colour scale is clipped to emphasise local variations.

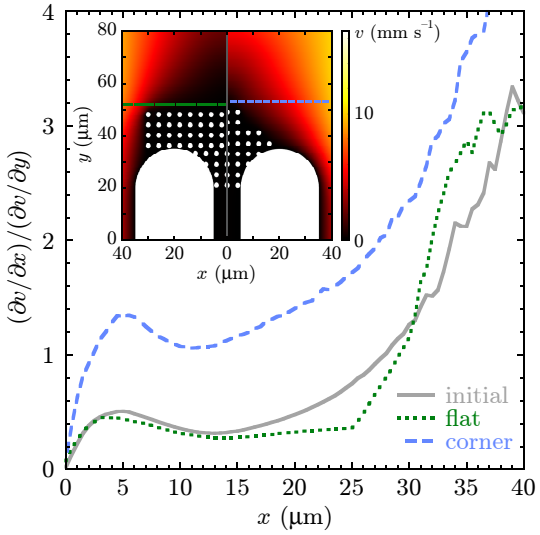

Fig. 6 Profile of the transverse-to-axial ratio of velocity gradients along the interception line, 3 µm upstream from the aggregate front, for three aggregate shapes (no aggregate, flat aggregate, corner-shaped aggregate). Inset: Velocity map computed around the pore for $v_0 = 8$ mm s^{-1} (corresponding to $Q = 20$ µL min^{-1} or Pe $= 1.7 \times 10^3$), covered by a flat (left half) or a corner-shaped aggregate (right half).

1.5 particle radius upstream of the deposition front (see section S2 in Supplementary Material†for more details, and Supplementary Figure S3†for examples of velocity and velocity gradient profiles along this line).

The axial and transverse velocity gradients characterise the axially- and transversally-oriented stresses (*i.e.*, the normal and tangential stresses if the flow was unidirectional), respectively. The ratio $(\partial v/\partial y)/(\partial v/\partial x)$ therefore compares, up to a constant multiplier, the lateral particle migration, that would divert an incident particle away from the obstacle, to its advection along the main flow axis, that would push it on the pore. The initial ($N = 0$) profile of this ratio along the interception line is plotted on Fig. 5 (solid line). Null on the centreline of the pore, it features a local maximum that coincides with the gap half-width ($x = 5$ µm $= w/2$) and a local minimum about 10 µm away, near the connection between the clog and the obstacle. In other words, an incident particle tends to be (i) strongly pushed forward if incoming along the centreline, (ii) pushed outwards if flowing within the pore entrance (gently near the edge of the clog, more firmly near the edge of the gap), and (iii) kicked away if flowing outside of this region.

How will deposited particles alter this pattern? The first particle is most likely to be captured on the centreline due to the purely axial pushing force. A particle captured at $x = 0$, as represented in light green in the left half of the inset on Fig. 5, in turn strongly increases the transverse velocity gradient near this axis, while slightly decreasing the local maximum at $x = w/2$ (green dotted line in Fig. 5), thus producing a plateau-like region of moderate lateral repulsion all over the curved part of the pore entrance ($x = 5$–20 µm). Subsequent deposition is therefore more likely within this region. The blue dashed line in Fig. 5 corresponds to a particle deposited at $x = 12$ µm, near the edge of the clog (Fig. 5, right half of the inset; the particle is depicted in light blue). The velocity gradient ratio locally becomes negative between the centreline and the captured particle, due to a reversal of the transverse component. Therefore, in this area a particle tends to be pushed inwards, favouring its capture right to the gap.

To summarise, particles captured along the centreline tend to favour subsequent captures on the sides of the pore, while particles captured on the sides in turn favour more central captures, up to filling a complete line of the growing front. This process may then repeat, explaining the fluctuating temporal patterns of flat growth [Fig. 4 (d)].

However, since one single particle alters the local flow pattern, the growing aggregate should even more. Figure 6 represents the $\partial_x v/\partial_y v$ profile for a flat (inset, left half; green dotted line) and a corner-shaped (right half; blue dashed line) aggregates; the initial case is also replotted for comparison (solid line). The main difference between the flat aggregate and the initial state resides in the appearance of a wide plateau, spanning almost the whole width of the aggregate. Comparatively to the initial state, the capture of a particle flowing near the aggregate edge is therefore more likely. This is consistent with the non-saturating growth of flat aggregates [Fig. 3 (b)] as the capture front does not narrow down so long as particles keep depositing at the edge. In fact, this plateau should even widen as particles are captured at the aggregate edge, in line with the observed increase of w^* over long times [Fig. 4 (b)].

The $\partial_x v/\partial_y v$ profile in the corner case is actually quite similar to the initial case, but amplified. Therefore, the lateral repulsion experienced by incident particles is always very strong, except

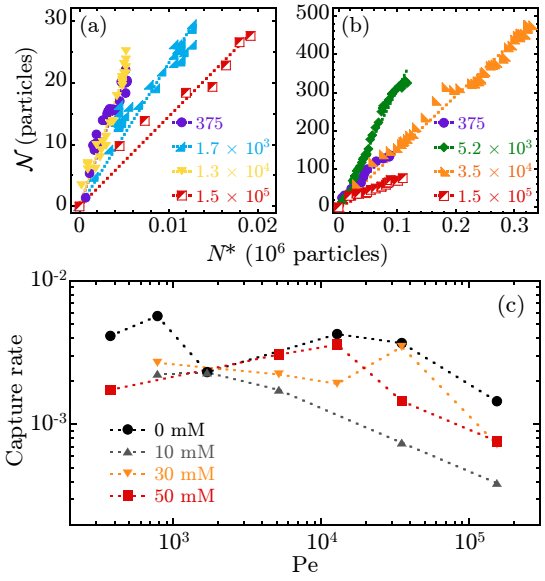

Fig. 7 (a, b) Growth dynamics of Fig. 3 rescaled as number of collected particles $\mathcal{N}$ *versus* the number of particles potentially captured, N^*. (a) $I = 0$ mM, (b) $I = 50$ mM. Dotted lines are linear fits. (c) Evolution of the particle capture efficiency (aggregate growth rate) with Pe for four different ionic strengths.

within a straight zone (less than two-particle wide). Particle accumulation is restricted to this area only. Aggregate growth should thus be spatially selective provided that a sufficiently wide, flat base was not built first to allow more lateral deposition.

Simulations of the flow pattern thus give a qualitative view of the deposition history at the single particle level, but do not explain the emergence of a particular shape. Understanding the observed equilibrium shapes requires to consider the effect of ionic strength, which will be discussed in section 5.

Note finally that the growth scenario described here remains specific to cases laterally unconfined, excluding by the way the clogging of microfluidic pores[14,15]. First, the lateral confinement in pores would indeed prevent particles from avoiding a growing aggregate; the capture probability would therefore strongly increase as the aggregate grows. This lateral confinement may also induce inertial effects, such as particle migration due to the convergence of streamlines. Second, within a pore aggregates grow orthogonally to the flow[14] and therefore experience anisotropic flow conditions, which may impact the capture efficiency.

3.2.3 Capture efficiency.

We now turn back to the growth dynamics at the pore scale. As noticed above, the aggregate growth rate $\mathrm{d}\mathscr{A}/\mathrm{d}N$ correlates very well with the effective capture width w^* while the aggregate grows [Fig. 4 (a–d)]. This correlation suggests that the particle capture efficiency, which *a priori* depends on Pe and I, remains constant during the aggregate growth and does not depend on the growth history. To estimate it, we first consider the number N^* of particles which have flowed through the effective capture front during the growth. At first order,

$$N^*(t+\Delta t) \simeq N^*(t) + \Delta N \frac{w^*(t)}{W}, \qquad (1)$$

with ΔN the number of particles flowing through a cross section $W \times h$ during the time interval Δt.

Besides, we also estimated the number of collected particles,

$$\mathcal{N} = \frac{\mathscr{A} h \phi_a}{V_p}, \qquad (2)$$

with V_p the volume of a particle and ϕ_a the average volume fraction in the aggregate, assumed as $\phi_a \sim 0.5$. Although we do not know the internal structure of the aggregate, this value close to the random loose packing allows for an order-of-magnitude estimate.

The growth dynamics can now be rescaled in terms of number of particles in the aggregate *versus* particles potentially captured, as represented on Fig 7 (a, b) for the data of Fig. 3. Remarkably, this rescaling makes all the growth dynamics linear, regardless of the aggregate shape; linear fits therefore give the average particle capture rate, that is plotted against Pe on Fig. 7 (c) for four different ionic strengths. Capture efficiencies are found in the order of few 10^{-3}, slightly increasing up to Pe $\sim 10^4$ then decreasing, down to a factor of about 4–5 compared to the maximum value. Besides, no clear dependence in ionic strength emerges from the data considered, although the series at 10 mM seems systematically lower. However, it must be kept in mind that potential variations in capture efficiency may be partly screened here since we assumed a value of ϕ_a common to all Pe and I. Typical volume fractions in disordered solids may actually vary depending on the formulating conditions, ranging from $\phi_a \sim 35$ % (dense colloidal gels under confinement[16]) to 64 % (random close packing). Nevertheless, this variability is not sufficient to disrupt the observed trend. The weak variation of capture efficiency with Pe and I therefore seems quite robust, considering the wide range investigated.

4 The low-shear regime: Aggregate growth over a sheltered pore

In the previous part, we demonstrated that the flow patterns near the pore entrance dictate the location of particle capture. We now investigate the effect of an obstacle located upstream of the pore, which creates a region of very low velocity in its wake and therefore reshape the flow pattern.

4.1 Low-shear zone

To evidence the wake effect on aggregate growth, we first varied the obstacle-to-pore distance, D, from 200 down to 50 µm. Representative images of the aggregates built for $Q = 20$ µL min^{-1} and $I = 0$ mM are shown on Fig. 8 (a), together with profiles illustrating the growth. As observed for single pores, the aggregate grows until a steady shape is reached. For large distances ($D \geqslant 150$ µm), only small aggregates build up, barely covering the whole obstacle width. Bringing the obstacle closer (100 µm or below), the aggregate becomes more substantial, taking a 'bowler hat' shape that fully covers the pore. This shape, rather rounded for $D = 100$ µm, progressively flattens at shorter distances.

As shown in the single pore case, the aggregate shape should be related to the flow pattern within the obstacle wake. Com-

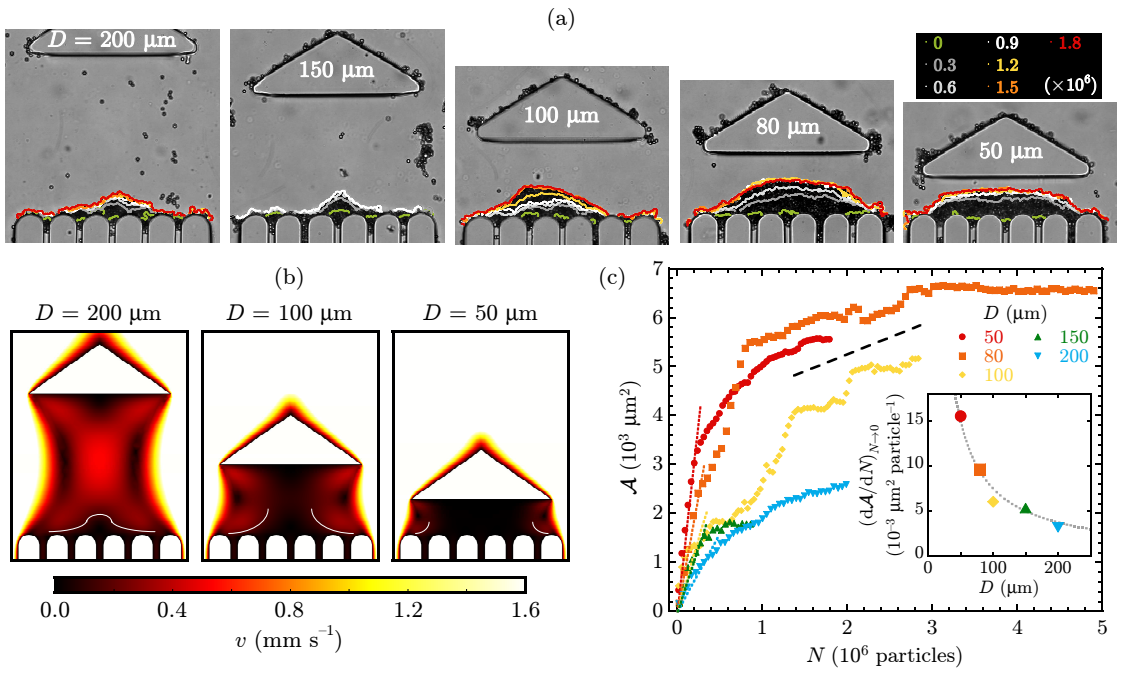

Fig. 8 Aggregation behind obstacles. (a) Growing influence of the obstacle when bringing it closer from the porous obstacle. Representative profiles corresponding to increasing N are superimposed to the images to illustrate the aggregate growth. (b) Calculated velocity maps in the wake of the obstacle for three obstacle-to-pore distances. The colour scale is clipped to emphasise local variations. The $v = 0.15$ mm s^{-1} velocity contour near the pore is depicted in white. (c) Growth dynamics. Each dynamics corresponds to a single aggregate growth; areas measured over two parallel sheltered pores typically varied by ± 10 %. The dotted lines are linear fits to the initial dynamics; the black dashed line indicates the subsequent growth trend (slope: 0.7×10^{-3} µm^2 particle^{-1}). Inset: evolution of the initial growth rate with D. The solid line is an inverse-law fit, drawn as a guide to the eye. Experimental parameters: $Q = 20$ µL min^{-1}, $I = 0$ mM; inflow velocity used in simulations: $v_0 = 8$ mm s^{-1}.

puted velocity maps are represented on Fig. 8 (b) for $D = 50$, 100 and 200 µm. As D decreases, a low-velocity area, identified as the dark zone in the image, grows and widens up covering almost the whole gap between the obstacle and the pore. Interestingly, the aggregate steady shape approximately coincides with the $v = 0.15$ mm s^{-1} velocity contour, where the velocity gradient starts to become more significant, which suggests that particle accumulation is favoured within a low-shear sheltered zone. The growth dynamics [Fig 8 (c)] strengthen this argument. As suggested by comparison of the respective profiles, the initial growth fastens with the size of the low-shear zone — initial growth rates actually fall onto a $1/D$ trend as shown in the inset. In this first stage, particles rapidly accumulate in the heart of the low-shear zone where erosion is not significant. The larger this zone, the more likely incident particles would feed it.

The growth then proceeds at a slower rate ($\sim 0.7 \times 10^{-3}$ µm^2 particle^{-1}, see dashed line), quite independent on D. In this regime, the aggregate is already mostly formed and particles carried by the tangential flow alongside may be progressively captured. Capture probability therefore only depends on the contour length of the aggregate, which is essentially the same in all cases considered here. Finally, a saturation, as seen beyond 3×10^6 particles for $D = 80$ µm, is reached when the shear-induced erosion balances this deposition process.

Lowering the electrostatic repulsion allows particles to bind more easily, favouring by this way the formation of cohesive aggregates. The erosion should therefore take place at higher critical shear rates when increasing the ionic strength. Consequently, for a given flow rate the low-shear zone should expand laterally, and aggregates should grow substantially at relatively large D. Figure 9 (a), showing aggregates grown for $I = 50$ mM and $D = 100$ µm for two flow rates ($Q = 20$ and 500 µL min^{-1}, corresponding to Pe $= 358$ and 8.2×10^3, respectively), illustrates this expansion if compared to the corresponding image on Fig. 8 (a). However, increasing the flow rate attenuates this expansion as the structure is distinctly smaller in the higher-Péclet case, yet still larger than without salt, and looks more rounded as was observed without salt for larger values of D.

Figure 9 (b) compares the growth dynamics in the 50 mM case, with $D = 100$ (left) or 50 µm (right), for $Q = 20$, 100 and 500 µL min^{-1} — the corresponding Pe are indicated; note that they do not significantly vary with D. Interestingly, the initial dynamics are similar, irrespective of D, and found close to that of $I = 0$ mM, $D = 50$ µm (trend reproduced as grey dotted line). Although this similarity may appear in contradiction with the $1/D$ trend observed in the no-salt case, it can actually be understood as resulting from the lateral expansion of the low-shear zone. Assuming a higher critical shear [the white line in the insets of Fig. 9 (b), left half, corresponds to the $v \sim 0.6$ mm s^{-1} contour], the low-shear zone indeed has the same width in the two cases, moreover fairly comparable to that found at $I = 0$ mM, $D = 50$ µm. It is therefore not surprising to get a similar dynamics at this stage of the growth.

Strongly increasing Pe rises the velocity gradient in the wake

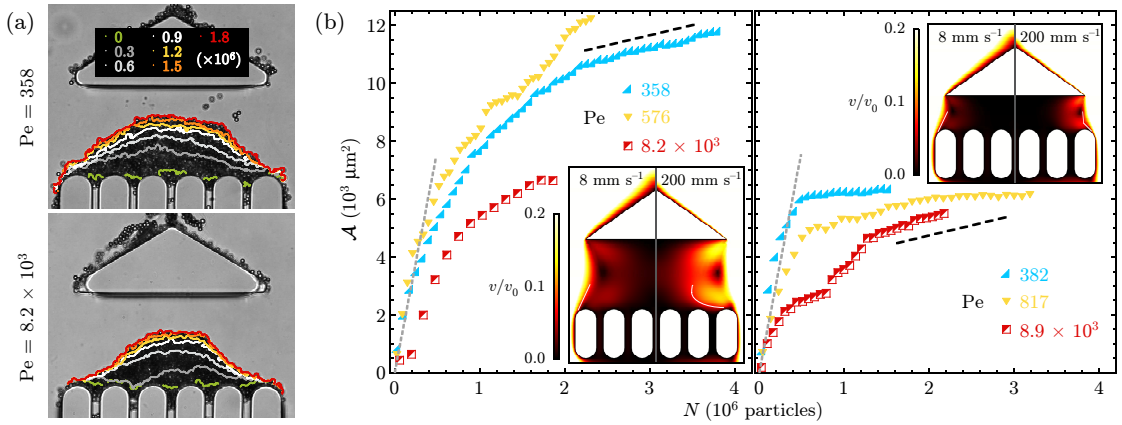

Fig. 9 Aggregation behind obstacles at high ionic strength ($I = 50$ mM). (a) Representative images of the aggregates built for two different Pe, $D = 100$ μm, with profiles corresponding to increasing N. (b) Growth dynamics for three values of Pe, corresponding to $Q = 20$, 100 and 500 μL min^{-1}; $D = 100$ (left) and 50 μm (right). Each dynamics corresponds to a single aggregate growth; areas measured over two parallel sheltered pores typically varied by less than 10 %. The dotted and dashed lines reproduce the initial and tangential deposition trends of Fig. 8 (case $D = 50$ μm), respectively. Insets show velocity maps for the two extreme flow rates considered here; white lines approximately delimit the low-shear zone. The colour scale is clipped to emphasise local variations and scaled so as to cover the same range in v/v_0.

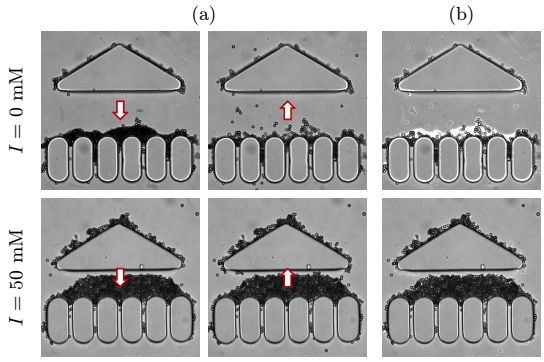

Fig. 10 Influence of the ionic strength on the aggregate cohesion. (a) Comparison of the aggregate shapes before (left column) and after (right) reversing the flow (arrows), for $I = 0$ (top row) and 50 mM (bottom). (b) Image subtraction of the two corresponding images in (a), highlighting the withdrawn area (in white).

of the obstacle, in a way similar to increasing its distance to the pore, and therefore reduces the low-shear zone [Fig. 9 (b), right half of the insets; the white line corresponds to the same v/v_0 as of the left-half case], especially in the $D = 100$ μm case. Again, the more rounded shape and the slower initial dynamics compared to those of lower Pe values both make sense in this view.

Finally, we should also consider the subsequent stage of growth dynamics. The tangential capture rate is actually similar to that estimated without salt (dashed lines on Figs. 8 and 9 have the same slope), though a slight increase with Pe may be noted. This independence of the capture rate with I is consistent with the trend featured on Fig. 7 (c).

4.2 Aggregate cohesion

The overall greater extent of the aggregates obtained at higher ionic strength is assumed to result from their better holding against shear. To check this hypothesis, we probed the influence of ionic strength on aggregate cohesion, by gently reversing the flow after the end of the experiment. Typical before-and-after images are represented on Fig. 10 (a). Without salt (top row), a major part of the aggregate has been withdrawn, only leaving particles stuck on the PDMS surface. This withdrawal occurs as soon as the flow reverses, independently of the obstacle-to-pore distance (Supplementary Movies 5 and 6†). Note that particles are sucked mostly one by one, although few doublets can be seen. This observation strongly suggests that aggregates formed in weak ionic strength conditions have a repulsive glass-like structure, and hold in place thanks to the pushing fluid on their boundary. This was also evidenced by monitoring the aggregate evolution after the flow was slowed down to nearly zero (no reversal), as seen in Supplementary Movie 7†. Due to thermal agitation, particles in the peripheral region of the aggregate jiggle around, whereas some rearrangements can be seen within the aggregate. Such behaviours were also observed by Ortiz *et al.* for truly 2D aggregates, also formed with highly-charged particles[8].

In contrast, in the 50 mM case (bottom row) the aggregate shape is preserved when the flow is stopped or reversed. Image subtractions [Fig. 10 (b)] confirm this qualitative difference between the high- and low-ionic strength cases. The aggregates built in high ionic strength conditions are therefore cohesive, as colloidal gels.

5 Discussion

We have first identified (section 3) four distinct aggregate shapes depending on the flow and ionic strength conditions (Fig. 2). These shapes are gathered on a phase diagram on Fig. 11. We have then (section 4) investigated more finely the effect of erosion on the final aggregate shape (Figs. 8 and 9). Finally, we have showed that the ionic strength dramatically alters the aggregate cohesion (Fig. 10).

In low ionic strength conditions, the strong electrostatic repulsion prevents particles from binding. The aggregates formed in these conditions are not cohesive and are only held stable by

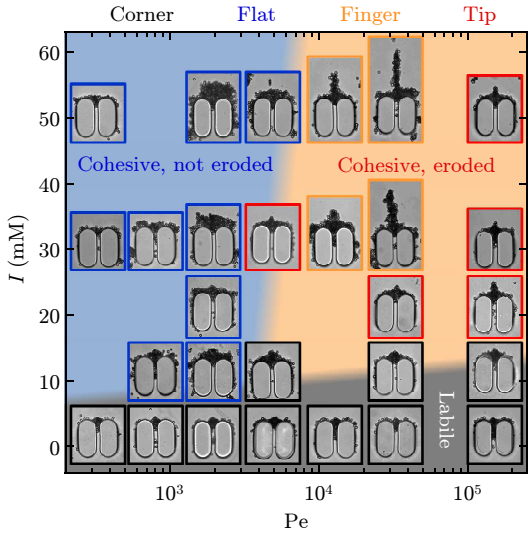

Fig. 11 Phase diagram in the (Pe, I) plane gathering the different aggregate shapes observed. Typical images of corner-, flat-, finger- and tip-shaped aggregates are framed in black, blue, orange and red, respectively.

the pushing flow. The strong velocity gradient near the pore entrance (see Fig. 5) will therefore detach particles captured in high velocity regions. This erosion thus determines the aggregate equilibrium shape, as observed in the sheltered case [see, for example, Fig. 8 (b)]. Over single pores, the 'corner' shape also matches the velocity contours near the pore entrance (Fig. 5). This sandpile-like shape is therefore expected in cases when particles do not have any contact, and is retrieved in the 'labile' region of the phase diagram (Fig. 11, dark grey area). It corresponds to the minimal shape that can be built under flow over a single porous obstacle: no deposition occurs once the equilibrium shape is reached, and its stability is granted by the imposed flow.

Screening the electrostatic repulsion allows the formation of cohesive aggregates due to irreversible particle binding. This will allow larger aggregates to grow as particles captured upon the aggregate boundaries may resist to the erosive flows further upstream of the pore, where the velocity gradients are stronger. In high ionic strength conditions, one may then distinguish two regions, depending on whether or not the erosion influences the aggregate shape.

At moderate flow velocity, the shear stresses at the aggregate boundary are not sufficient to detach particles, which can therefore cover the sides of the obstacle or aggregate, and allow the subsequent capture of particles over a wide front (see Fig. 6). This is illustrated in the top left quadrant of the phase diagram ($\mathrm{Pe} \lesssim 5 \times 10^3, I \gtrsim 10$ mM, blue area), where 'flat' aggregates are found. Note that even a moderate ionic strength (10 mM) may actually screen the electrostatic repulsion enough for some particles to bind, as they may cover the whole width of the pore at low Pe; smaller, corner-shaped aggregates are retrieved at higher Pe.

At higher flow velocity (top right quadrant of the phase diagram, orange area), the erosion plays a significant role. Particles that may be captured on the sides of the aggregate will be detached by the flow. Erosion thus selects the centreline of the pore as privileged growth direction, which in turn prevents lateral particle capture due to the reshaping of the flow field (see Fig. 6, corner case). Elongated 'finger' aggregates then progressively build along the centreline of the pore where all particle depositions take place; note that increasing Pe produces longer and thinner aggregates, which illustrates that this spatial selectivity strengthens with the erosion. At even higher Pe, particles start to detach even on the centreline, preventing the growth of very long aggregates. This regime corresponds to the 'tip' shape. Although this shape resembles to the corner, they are clearly distinct. First, tips are cohesive, while corners are not — this can be evidenced be the occurrence of internal rearrangements due to the permeation flow in the corner case only, compare Supplementary Movies 1 and 4†. Second, their growth dynamics are different: while a corner does not grow any more once its equilibrium shape is reached, a tip keeps capturing new particles as erosion drag the extreme ones out.

6 Concluding remarks

We experimentally investigated the coupling between hydrodynamic and colloidal interactions on the accumulation of microparticles over porous obstacles. More specifically, by flowing colloidal suspensions of tunable ionic strength into microfluidic channels, we studied the formation of dense structures on obstacles of tunable geometry, over almost three orders of magnitude in Péclet number. We observed a large diversity of geometrical shapes, distinguishing several localised and more uniform growth modes, and explained this diversity by the interplay between shear drag and colloidal interactions.

On the one hand, the flow pattern at the single particle level drives the trajectory of the incident particles and therefore their deposition dynamics. Growing structures in turn modify the local flow conditions, which directs further particle accumulation. Besides, the particle capture efficiency hardly depends on the Péclet number or the ionic strength in the investigated range.

On the other hand, the cohesion of the structure dictates its equilibrium shape, as it may allow a particle deposited on the aggregate sides to hold under flow. Aggregates built in low ionic strength conditions are indeed held in place by the pushing flow, whereas those formed at high ionic strength are cohesive. This stability may allow the growth of the structure over a wide front, whereas erosion selects a localised growth mode along the centreline of the pore. These labile and cohesive structures may be compared to polarised layers and filtration cakes that grow by retention on membranes [17,18]. Further investigation of these dense states with microfluidic tools could focus on their structural evolution under controlled flow. More specifically, confocal microscopy would give access to the local microstructure, and shed light on their ageing dynamics under vanishing Pe [19]. Conversely, strong flows through the structure may induce non-linear rheological responses [9,20]. Such studies might eventually find industrial applications in microfiltration, by allowing new strategies to prevent membrane fouling.

7 Acknowledgements

The authors wish to thank Alexandre Schmit and Benjamin Dersoir for their help in image processing and computational modelling, and Serhane Zerdane for early-stage experiments. This work was supported by the Agence Nationale de la Recherche through grant number ANR-12-JS09-0003. M. A. would like to thank the support of the Région Languedoc-Roussillon (chercheur d'avenir 2012) and the Labex NUMEV (convention ANR-10-LABX-20).

References

1 R. Piazza, S. Buzzaccaro, E. Secchi and A. Parola, *Soft Matter*, 2012, **8**, 7112–7115.

2 G. Brambilla, S. Buzzaccaro, R. Piazza, L. Berthier and L. Cipelletti, *Phys. Rev. Lett.*, 2011, **106**, 118302.

3 R. D. Deegan, O. Bakajin, T. F. Dupont, G. Huber, S. R. Nagel and T. A. Witten, *Nature*, 1997, **389**, 827–829.

4 Á. G. Marín, H. Gelderblom, D. Lohse and J. H. Snoeijer, *Phys. Rev. Lett.*, 2011, **107**, 085502.

5 Y. Kusaka, J. F. L. Duval and Y. Adachi, *Environ. Sci. Technol.*, 2010, **44**, 9413–9418.

6 P. Bacchin, A. Marty, P. Duru, M. Meireles and P. Aimar, *Adv. Colloid Interface Sci.*, 2011, **164**, 2–11.

7 P. Bacchin, Q. Derekx, D. Veyret, K. Glucina and P. Moulin, *Microfluid. Nanofluid.*, 2014, **17**, 85–96.

8 C. P. Ortiz, R. Riehn and K. E. Daniels, *Soft Matter*, 2013, **9**, 543–549.

9 C. P. Ortiz, K. E. Daniels and R. Riehn, *Phys. Rev. E*, 2014, **90**, 022304.

10 J. N. Israelachvili, *Intermolecular and Surface Forces (Third Edition)*, Academic Press, San Diego, 2011.

11 D. C. Duffy, J. C. McDonald, O. J. A. Schueller and G. M. Whitesides, *Anal. Chem.*, 1998, **70**, 4974–4984.

12 P. Tabeling, *Introduction à la microfluidique*, Belin, Paris, 2003.

13 W. S. Rasband, *ImageJ*, U. S. National Institutes of Health, 1997–2014, http://imagej.nih.gov/ij/.

14 B. Dersoir, M. Robert de Saint Vincent, M. Abkarian and H. Tabuteau, *Microfluid. Nanofluid.*, accepted.

15 H. M. Wyss, D. L. Blair, J. F. Morris, H. A. Stone and D. A. Weitz, *Phys. Rev. E*, 2006, **74**, 061402.

16 F. Boulogne, L. Pauchard, F. Giorgiutti-Dauphiné, R. Botet, R. Schweins, M. Sztucki, J. Li, B. Cabane and L. Goehring, *EPL (Europhysics Letters)*, 2014, **105**, 38005.

17 J. C. Chen, Q. Li and M. Elimelech, *Adv. Colloid Interface Sci.*, 2004, **107**, 83 – 108.

18 S. S. L. Peppin, J. A. W. Elliott and M. G. Worster, *J. Fluid Mech.*, 2006, **554**, 147–166.

19 B. Abou, D. Bonn and J. Meunier, *Phys. Rev. E*, 2001, **64**, 021510.

20 C. W. MacMinn, E. R. Dufresne and J. S. Wettlaufer, *Phys. Rev. X*, 2015, **5**, 011020.

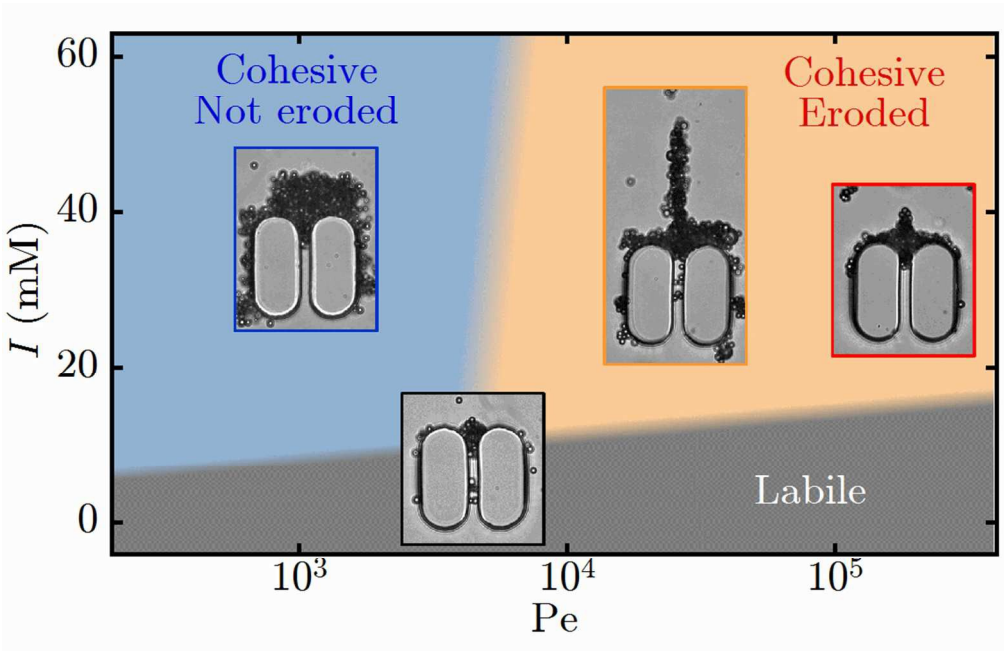

Colloidal interactions and shear forces compete to drive the accumulation of colloidal particles over porous obstacles, resulting in a large diversity of aggregate shapes.
402x260mm (72 x 72 DPI)